Available online at www.sciencedirect.com

ScienceDirect

Ceramics International 40 (2014) 10237–10246

CERAMICS INTERNATIONAL

www.elsevier.com/locate/ceramint

Mechanical properties of $Ca_3Co_4O_9$ bulk oxides intended to be used in thermoelectric generators

Driss Kenfaui[a,b,*], Moussa Gomina[a], Daniel Chateigner[a], Jacques G. Noudem[a]

[a]CRISMAT, UMR 6508 ENSICAEN/CNRS, LUSAC, Université de Caen Basse-Normandie, 6 Bd Maréchal Juin, 14050 Caen Cedex 04, France
[b]Institut Jean Lamour – CP2S, UMR 7198 CNRS – Université Loraine, Parc de Saurupt CS 50840, F-54011 Nancy, France

Received 23 January 2014; received in revised form 2 February 2014; accepted 26 February 2014
Available online 7 March 2014

Abstract

The lamellar thermoelectric (TE) oxides $Ca_3Co_4O_9$ (Ca349) are promising candidates for energy conversion in a temperature range of 300–1200 K in air. To be well-suited for being integrated in TE devices, Ca349 bulk materials must show high mechanical reliability to withstand the assembly constrains and in-service conditions. In the aim of optimizing TE performances of these materials, specimens were elaborated by using Hot-Pressing (HP) and Spark Plasma Sintering (SPS). Indentation measurements were operated on these ceramics using both micro-hardness testing and depth-sensing nano-indentation. Fracture characteristics were assessed by 3 point bending tests. Nano-hardness (nH), elastic modulus (E), strength (σ_R) and fracture toughness (K_{Ic}) were shown to drastically enhance versus the pressures P_{HP} and P_{SPS} applied during HP and SPS treatments, respectively, which is ascribed to higher densification and, to a lesser extent, to the texture strengthening and grain boundary density decrease in the direction perpendicular to the pressing axis. The contribution to micro-hardness (μH) of both later factors was estimated to ~30% for the hot-pressed sample under $P_{HP}=30$ MPa which depicted ($nH_{xy}=2.1\pm0.4$ GPa, $E_{xy}=56\pm4$ GPa) and ($nH_z=2.3\pm0.2$ GPa, $E_z=85\pm5$ GPa) in its respective planes perpendicular and parallel to the pressing axis, revealing an anisotropy of the elastic modulus. It presented $\sigma_R=251\pm12$ MPa and $K_{Ic}=2.3\pm0.4$ MPa $m^{1/2}$. Although the lower size of the intrinsic flaws was found for the HP materials, the largest mechanical characteristics were achieved by SPS under $P_{SPS}\geq50$ MPa. The elastic recovery H/E of Ca349 ceramics was found among the highest ratios reported for oxides and one order of magnitude larger compared to the half-Heusler or skutterudites potential TE materials.

Keywords: C. Mechanical properties; $Ca_3Co_4O_9$ thermoelectric oxides; Spark plasma sintering; Texture; Fracture toughness

1. Introduction

Emerging ecological awareness and increasing concern for energy needs have boosted progress in materials and technology for thermoelectric (TE) energy conversion in the last two decades. TE generators are being considered for scavenging a part of enormous amount of unused waste heat, produced by automobiles and several industrial processes, to generate electric power [1]. Development projects are already underway to change the alternator in cars with a TE generator mounted on the exhaust stream, thereby enhancing fuel efficiency [1,2].

TE devices contain many material couples consisting of n-type and p-type TE elements connected electrically in series and thermally in parallel. A TE generator uses heat flow across a temperature gradient to power an electric load through an external circuit. The temperature difference provides a voltage from the Seebeck effect [3] while the heat flow drives the electrical current, which therefore determines the power output [1]. The efficiency of a TE device generally improves by increasing the TE material figure of merit $ZT=S^2T/\rho\kappa$ (T: temperature, S: Seebeck coefficient, ρ: electrical resistivity, and κ: thermal conductivity) [4]. A great deal of research has been then mostly focused on the transport properties in order to

*Corresponding author at: Université de Caen Basse-Normandie, UMR 6508 ENSICAEN/CNRS, LUSAC, Laboratoire CRISMAT, 6 Bd Maréchal Juin, 14050 Caen Cedex 04, France. Tel.: +33 231 4513 66; fax: +33 231 95 16 00.
E-mail address: driss.kenfaui@live.fr (D. Kenfaui).

http://dx.doi.org/10.1016/j.ceramint.2014.02.112
0272-8842/

maximize ZT [1,5–11]. Figure of merit ($ZT > 1$) values making TE devices competitive have been achieved for several TE components, but there are still very little reports on their mechanical and thermal properties, although such information is essential for the sustainability of TE generators envisaged to be potentially used in harsh environments such as the internal combustion engines of cars. Indeed, these devices will be subjected to mechanical loading and vibration and extreme thermal cycling and shock in consequence of in-service conditions.

Layered cobalt oxides $Ca_3Co_4O_9$ (Ca349) are considered to be among the most expected material candidates for the aforementioned applications because they possess fairly good TE performances, resist oxidation in air, are thermally and chemically stable at high temperature, and do not exhibit any polluting or toxic character [5,6,12,13]. Prototype TE generators, fabricated exclusively from oxides, have been reported [14–18]. Ca349 materials have been used as *p*-type TE elements made by slicing and cutting conventional sintered samples that we have recently shown to possess poor mechanical properties [19,20]. That would make them too weak to withstand in-service conditions without failure. Reinforcement of the mechanical properties of Ca349 materials, as well as improvement of their efficiency ZT, is hence vital before these can be seriously considered for potential applications. A clear understanding of their mechanical behavior is as well required for their reliable integration together with other materials constituting the TE device. To minimize undue stress to the device, the *p*-type and *n*-type TE elements should possess similar thermal expansion coefficients and elastic modulus. The fabrication of TE device involves the machining of several hundred (or more) individual TE elements. Such machinability as well as wear resistance of material was reported to be governed by the hardness [21–25] which is linked to other mechanical properties including compressive strength [26,27], fracture toughness [28] and Young's modulus [29]. The mechanical characteristics are needed for TE devices design as well as for the induced stress analysis by the finite element method.

In the efforts to diminish the resistivity of the Ca349 bulk compound toward the development of TE elements with high thermal conversion efficiency, samples were fabricated by using Conventional Sintering (CS), Hot-Pressing (HP) and Spark Plasma Sintering (SPS) methods [21,22]. In the present work, the mechanical properties, viz. micro- and nano-hardness, Young's modulus, strength and fracture toughness are assessed for the processed Ca349 materials. The dependence of these properties on the resulting microstructural features and texture strength is widely explored. The mechanical characteristics of Ca349 materials are compared to other oxides, skutterudites, lead-antimony-silver-telluride (LAST) and half-Heuslers, TE materials reported to be as well potential candidates for energy conversion applications.

2. Experimental procedure

2.1. Materials

Conventional solid-state synthesis of Ca349 powders are described in detail elsewhere [19,20,30,31]. The starting precursors $CaCO_3$ and Co_3O_4 were weighed in the proper stoichiometric ratios and mixed in an agate ball mill before being calcined in air at 900 °C for 24 h to decompose the carbonates, thereby purifying the Ca349 phase. After regrinding, a first series of five 3–5 mm – thick and 25 mm – diameter pellets was elaborated by uniaxial cold-pressing Ca349 powders under 60, 80, 95, 160 and 200 MPa followed by CS treatment at 920 °C for 24 h where no uniaxial pressure was applied. The resulting relative percent densities are 58.7%, 60%, 60.9%, 64.6% and 66.3%, respectively.

A second series of pellets initially cold-pressed under 95 MPa was further treated using HP processing as described

Table 1
Microstructural, textural and mechanical characteristics of the hot-pressed Ca349 bulk materials under various applied uniaxial pressures P_{HP} at 920 °C for 24 h.

Uniaxial pressure P_{HP} (MPa)	**0**	**5**	**13**	**20**	**30**
Microstructural–textural characteristics					
Sample thickness (mm)	4.45	2.2–2.5	1.2–1.5	0.6–0.9	0.4–0.6
Relative percent densification (%)	60	90.5	94.8	95.1	96
Grain length (μm)	≤ 5	≤ 9	≤ 12	≤ 14.5	≤ 17
Grain thickness (μm)	≤ 5	–	≤ 0.18	–	≤ 0.12
Max. of {001} poles (mrd)	3.48	7.82	9.28	15.36	22.15
Mechanical characteristics					
μH_{xy} (GPa)	0.12 ± 0.01	–	–	–	1.3 ± 0.1
nH_{xy} (GPa)	0.11 ± 0.03	1.5 ± 0.4	2 ± 0.3	1.9 ± 0.3	2.1 ± 0.4
nH_z (GPa)	–	1 ± 0.15	2.2 ± 0.2	2 ± 0.15	2.3 ± 0.2
nH_z/nH_{xy}	–	0.67	1.07	1.03	1.11
E_{xy} (GPa)	10 ± 2	53 ± 8	52 ± 3	53 ± 4	56 ± 4
E_z (GPa)	–	53 ± 3	77 ± 4	74 ± 3	85 ± 5
E_z/E_{xy}	–	1.01	1.47	1.39	1.53
σ_R (MPa)	18.4 ± 0.5	198 ± 8	234 ± 6	254 ± 9	251 ± 12
K_{Ic} (MPa $m^{1/2}$)	0.40 ± 0.02	1.9 ± 0.2	2 ± 0.3	2.1 ± 0.1	2.3 ± 0.4

elsewhere [19,30]. The pellet was set in a home-made furnace between two 0.125 mm – thick silver sheets to prevent an undesirable reaction with the alumina bearing plates during HP treatment. The material was thereafter heated up to the dwell temperature of 920 °C maintained for 24 h under an uniaxial pressure P_{HP} which was varied from 0 to 30 MPa to investigate the hot-pressing effect on the microstructure of the Ca349 ceramics. The pressure was removed before cooling to avoid material cracking. The samples thickness monotonously decreased as P_{HP} was increased (Table 1). An applied pressure larger than 30 MPa led to too thin samples, impractical later for further manipulations.

Otherwise, a third series of Ca349 samples was prepared using Spark Plasma Sintering (SPS). The powders were treated in vacuum (10^{-3} bar) in the SPS apparatus (Model: HP D 25/1, Fine Ceramics Technologies (FCT), Germany). For each sample, 3 g of Ca349 powders were loaded in graphite die with an inner diameter of 20 mm. A pulsed electric current (2500 A, 4 V) was injected through the die to heat the material up to the dwell temperature of 900 °C while maintaining it under an uniaxial pressure P_{SPS} for 2 min. To investigate the microstructure evolution of the bulk Ca349 materials, P_{SPS} was varied from 0 to 100 MPa. After SPS treatment, the as-prepared samples (thickness ~2 mm) were moderately heated at 600 °C for 2 h before being polished to remove the graphite foil used during SPS sintering.

A pellet, obtained upon cold-pressing under 95 MPa followed by CS sintering at 920 °C for 24 h without uniaxial pressure, is taken as reference sample for second and third series.

2.2. Microstructural and textural characterizations

The relative percent density of the bulk Ca349 materials was computed by comparing the samples density measured *via* the Archimedes method (KERN & Sohn GmbH, Baligen, Germany) to the theoretical one reported for the Ca349 phase [13]. The microstructure was investigated using a Carl Zeiss (Supra 55, Oberkochen, Germany) Scanning Electron Microscope (SEM). The chemical composition and texture were investigated using X-ray diffraction on a 4-circle diffractometer setup equipped with a Curved Position Sensitive detector (CPS120 from INEL SA), and operating with a monochromatised Kα-Cu radiation [32], within the combined analysis formalism [33] implemented in the MAUD software [34]. Such methodology, described elsewhere [19,20,30,31], enables to quantify the texture of the samples from cyclic Rietveld refinement of 13 diagrams measured every 5° in tilt angle χ (sample orientation) at an incident angle of the X-ray beam on the sample of ω=20°. The recalculated pole figures are normalized into multiples of a random distribution (mrd), a unit which depends solely on the crystallites orientation. Thus, a sample without preferred orientations depicts uniform pole figures with 1 mrd levels, whereas a textured sample shows pole figures with maxima and minima of orientation densities spanning from 0 mrd (absence of crystals oriented in this direction) to infinity (for a single crystal on few directions). Such normalized pole figures are computed from the orientation distributions (OD) of crystallites, refined using the E-WIMV formalism [35] after extraction of the peak intensities during the Rietveld cycles.

The Ca349 supercell definition [36] was used during these refinements and a sample reference frame chosen in order that the direction of pressures (P_{HP} and P_{SPS}) application corresponds to the centre of our pole figures.

2.3. Mechanical characterizations

2.3.1. Micro-hardness testing and depth-sensing nano-indentation

Using a Zwick mechanical testing device, a course of Vickers indentation (micro-indentation) tests were performed in ambient air on polished surfaces of the samples to assess the micro-hardness, μH, of the Ca349 ceramics. The loading time was set at 15 s and the micro-hardness, μH, calculated from the applied load, P, and the diagonal lengths a_1 and a_2 of the indentation imprint according to the following formula [37]:

$$\mu H = \frac{2(\sin 136^\circ/2)P}{(a_1 a_2)} \quad (1)$$

Instrumented depth-sensing nano-indentation tests were carried out on the samples using a Nano Indenter® XP (MTS Systems Corporation, Eden Prairie, MN, USA). This system produces indentation loadings sensitive to ±1 μN and yields depth-sensing measurements within ±0.01 nm. For each test, a batch of nine imprints, ordered in a 3 × 3 array, were introduced using a Berkovich tip diamond indenter on the polished surfaces with a 50 μm mesh to avoid the interaction between the deformed areas. The maximum penetration depth was set at 2000 nm. After unloading, the recorded load–displacement data were used to compute nano-hardness and elastic modulus. The nano-hardness nH is computed such that

$$nH = \frac{P_{max}}{A} \quad (2)$$

where P_{max} refers to the load at the maximum penetration depth h, while A is the projected contact area between the indenter and the sample at P_{max}.

The elastic modulus, E, is determined using the formula

$$E = \frac{(1-\nu^2)}{1/E_r - (1-\nu_i^2)/E_i} \quad (3)$$

where E_i is the elastic modulus of the indenter while ν and ν_i are the respective Poisson's ratios of the sample and indenter. E_r refers to the reduced modulus defined as

$$E_r = \frac{\sqrt{\pi} S_h}{2\beta\sqrt{A}} \quad (4)$$

β is a factor depending on the geometry of the indenter with β=1.0615 for a Berkovich tip [38], and $S_h = \frac{dP}{dh}$ refers to the elastic stiffness of the specimen-indenter contact [39].

In the nano-indentation tests on Ca349 materials, we used the continuous stiffness measurements (CSM) option of the Nano Indenter1 XP to evaluate the elastic contact stiffness S_h all along the loading path of the load-penetration curve.

2.3.2. Flexural tests

The fracture stress σ_R was determined for the Ca349 materials in ambient air using 3 point bending tests. The maximum tensile stress on the bottom surface of the specimen is calculated from the specimen thickness, the bending moment and the moment of inertia of the cross section. The fracture stress σ_R is therefore given by

$$\sigma_R = \frac{3}{2}\frac{F_R L}{BW^2} \quad (5)$$

for a parallelepiped specimen, where F_R is the fracture load, L the span, B and W are the specimen width and height, respectively.

Bars for flexural tests were cut from the samples with almost the same $W \sim 2$ mm thickness, $B \sim 3$ mm width and $L = 12$ mm span to enable a comparison among strength values. The load was applied in the direction parallel to the pressing axis during the processing.

Fracture toughness measurements were performed on single-edge notched bend (SENB) specimens with relative notch length of $a_0/W \sim 0.33$ introduced using a 50 μm thick saw. The fracture toughness is hence computed according to the following formula:

$$K_{Ic} = Y\sigma_R\sqrt{a_0} \quad (6)$$

Y is a polynomial function of the a_0/W ratio that takes into account the finite size of the specimen. This factor depends on the geometry of the specimen and the loading configuration. For a SENB specimen, Y values are tabulated versus a_0/W and L/W ratios. Here, the predominant fracture mode is the one corresponding to a crack opening under a normal tensile stress perpendicular to the notch plane, commonly known as mode I.

3. Results and discussion

3.1. Hardness and elastic modulus

3.1.1. $Ca_3Co_4O_9$ processed by CS and HP

Fig. 1 depicts the evolution of the micro-hardness μH_{xy} of isotropic Ca349 ceramics of the first series as a function of the achieved densification. The mean μH_{xy} reported for each sample is an average over the 10 imprints on (x,y) planes of the samples (Fig. 2) introduced by applying a load of 2 N parallel to the cold-pressing axis. A linear increase of the μH_{xy} values versus the relative density is observed up to around 66%, our instrumental limit for the cold-pressing equipment. Denser isotropic Ca349 ceramics are hardly achievable without inducing a texture because of the layered character of the crystal structure [13] which results in lamellar grains [19,20,30,31]. The micro-hardness μH_{xy} of highly densified (96%) Ca349 ceramics with randomly oriented grains was then estimated at 0.9 GPa by extrapolation of the values associated to the five aforementioned specimens (Fig. 1).

Micro-hardness measurements were carried out as well on strongly textured and 96%-densified Ca349 samples (Table 1) processed using HP under 30 MPa. The imprints on (x,y) plane of the sample (Fig. 2) were obtained by applying a load of 5 N

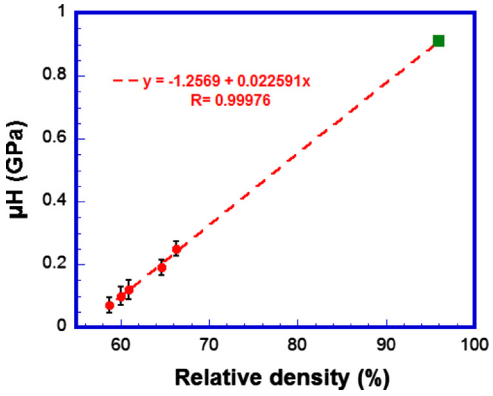

Fig. 1. Micro-hardness (μH_{xy}) versus the relative percent density of the conventional sintered Ca349 materials. μH_{xy} is estimated for a highly (96%) dense isotropic Ca349 ceramic.

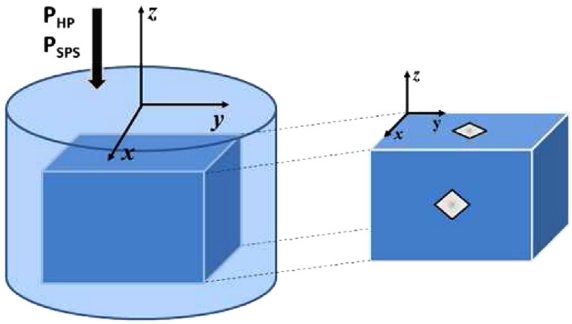

Fig. 2. Schematic showing the sample planes on which imprints were introduced during micro- and nano-indentions tests.

parallel to the direction of pressure P_{HP} application. The corresponding μH_{xy} value raises from 0.12 ± 0.01 GPa for the reference sample to 1.3 ± 0.1 GPa for the textured one, highlighting a hardening of more than one order of magnitude predominantly ascribed to the densification and, to a lesser extent, to the texture strengthening and the grain length increase (Table 1) inducing a reduction in the (x,y) plane grain boundary density (GBD). Indeed, while the reference sample evidences a strongly porous microstructure (60% of the theoretical density) with small grains loosely assembled and randomly distributed (Fig. 3a) in keeping with the weak texture strength (Fig. 3b), the sample processed by HP under 30 MPa appears more homogenous and presents much denser microstructure with largely grown platelets compactly stacked up along the pressing axis and highly oriented (Fig. 3e). The maximum of the {001} poles is around 22 mrd (Fig. 3f), the strongest texture recorded hitherto on Ca349 materials.

The crystallographic orientation and GBD decrease contributions to the micro-hardness is quantified to about 31% by comparing the μH_{xy} value of the textured material to the estimated hardness of the isotropic ceramics at the same relative density (96%).

Nano-hardness, nH, and Young's modulus, E, were determined for Ca349 samples *via* nano-indentation tests. In order to check eventual anisotropy influence on these mechanical properties in the samples textured by HP, imprints were

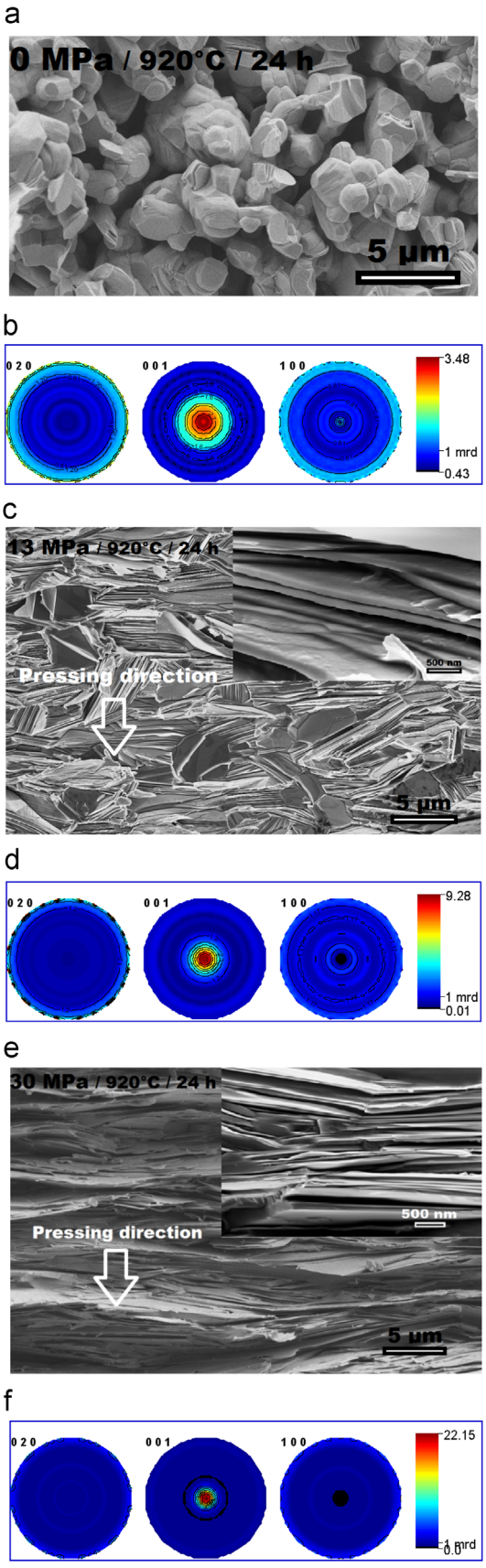

Fig. 3. SEM micrographs of the microstructure, and {020}, {001} and {100} pole figures obtained for (a and b) the Ca349 conventionally sintered (CS) sample (reference) and the hot-pressed ones under pressures PHP of (c and d) 13 and (e and f) 30 MPa. Insets evidence the thickness of the platelets achieved under these pressures and how the latters are aligned and stacked up along the hot-pressing axis.

introduced on (x,y) and $(x,z)/(y,z)$ planes of the sample (Fig. 2) by applying the load parallel (nH_{xy} and E_{xy}) and perpendicular (nH_z and E_z) to the direction of pressure P_{HP} application, respectively.

The average nH_{xy}, nH_z, E_{xy} and E_z values of the Ca349 samples treated by HP under various pressures P_{HP} up to 30 MPa are regrouped in Table 1. The nano-hardness drastically improves with P_{HP}. Indeed, nH_{xy} raises from 0.11 ± 0.03 for the reference sample to 1.5 ± 0.4 GPa under an effect of a moderate pressure P_{HP} as high as 5 MPa. In this P_{HP} range, the Ca349 ceramics are markedly densified from 60% to 90.5% whereas the texture strength only goes from 3.48 to 7.82 mrd, emphasizing that nH_{xy} increase mainly derives from the densification in accordance with the micro-hardness. The texture as well as the reduction in (x,y) plane GBD (Table 1) secondarily contributed to the nH_{xy} enhancement.

Beyond 5 MPa, the samples display similar nH_{xy} values to within $\pm$ one standard deviation in data although the texture strength and the grains length notably increase (Table 1), endorsing hence the primacy of the densification effect on nH_{xy}. nH_{xy} reaches 2.1 ± 0.4 GPa for the hot-pressed material under 30 MPa, corresponding to 19 fold the reference sample. Here, it is worth noting that this hardness value is 3.7 and 2.1 fold the hardest compounds $Ba_{0.075}Sr_{0.025}Yb_{0.1}Co_4Sb_{12}$ and $Zr_{0.5}Hf_{0.5}Ni_{0.6}Pd_{0.4}Sn_{0.99}Sb_{0.01}$ reported so far for the hot-pressed skutterudite [40] and half-Heusler [41,42] TE materials, respectively.

The nano-hardness nH_z was found to be higher than nH_{xy} for P_{HP} higher than 13 MPa, due to more significant texture strengthening (beyond 9 mrd) as can be observed in Fig. 3c–f. nH_Z attains 2.3 ± 0.2 GPa for a pressure P_{HP} of 30 MPa, which is 21 fold the reference sample. Under such pressure, the Ca349 ceramics display a hardness anisotropy $H_z/H_{xy} = 1.11$, which can be overlooked owing to the nH_{xy} and nH_z values similarity to within $\pm$ one standard deviation in data.

On the other hand, while the isotropic material (reference sample) presents μH_{xy} and nH_{xy} of around 0.11 GPa, the nH_{xy} value of the sample textured by HP under 30 MPa shows an increase of 38% compared to the μH_{xy} one, which is probably tied to the more localized character of nano-indentation measurements. Bearing in mind the larger grain length (17 µm) for the textured sample, this result suggests that nH_{xy} values are closer to those of the grains, whereas those of μH_{xy} correspond to the macroscopic values taking into account the grain boundaries and porosity effects. A discrepancy between micro- and nano-hardness was also reported by Yang et al. [43] on $Ti(C_xN_{1-x})$, $Zr(C_xN_{1-x})$ and $Hf(C_xN_{1-x})$ compounds.

The elastic modulus, E, depends as well on the applied pressure P_{HP}. E_{xy} raises from 10 ± 2 to 53 ± 8 GPa as P_{HP} is increased from 0 to 5 MPa, due to the same factors noted for nH_{xy}.

E_{xy} reaches 56 ± 4 GPa for the materials processed under 30 MPa, i.e. 5 times larger compared to the reference sample. This value is comparable to the Young's modulus reported on $AgSbPb_{18}Te_{20}$ LAST compound, but, about 2 fold the values recorded on $Ag_{0.9}SbPb_{18}Te_{20}$ and $Ag_{0.7}SbPb_{18}Te_{20}$ ones treated by HP as well [44]. However, it remains more than 2 and 4 fold lower compared to the largest stiffness reported on the hot-pressed $Ce_{0.9}Fe_{3.5}Co_{0.5}Sb_{12}$ (also on $Co_{0.95}Pd_{0.05}Te_{0.05}Sb_{12}$) and $Zr_{0.5}Hf_{0.5}CoSb_{0.99}Sn_{0.01}$ compounds for the skutterudite [45] and half-Heusler [41,42] TE families, respectively. It is relevant to note that the reported compounds cited here possess larger bulk density (> 98%).

E_z displays a steeper increase than E_{xy} tied to the texture strengthening (Fig. 3e and f), and attains 85 ± 5 GPa for the sample hot-pressed under P_{HP}=30 MPa. The stiffness anisotropy E_z/E_{xy} appears more pronounced than for the hardness and increases with P_{HP} up to 1.53 for the latter.

3.1.2. $Ca_3Co_4O_9$ processed by SPS

Fig. 4 depicts SEM micrographs of fractured surfaces of the samples consolidated by SPS under pressures, P_{SPS} of 30, 50 and 75 MPa. For P_{SPS}=30 MPa (Fig. 4a), the sample exhibits much stronger bulk density (98.3%) compared to the reference sample (Fig. 3a), and the grains show roughly platelet-like shape with a tendency to be oriented and stacked perpendicularly to the pressing direction. However, limited porous zones comprising smaller and more isotropic grains persist, which is suggestive of an uncompleted material sintering. Under P_{SPS}=50 MPa (Fig. 4b), the sample is almost fully densified (99.6%) with no porous zone.

Table 2 shows neither a significant reinforcement of the texture nor an increase of the mean grain size with the P_{SPS} pressure as can be seen from Fig. 4a–c as well. Such limitation probably stems from the increasing lateral pressure applied by the die walls on the sample during the uniaxial P_{SPS} pressing. Since the sample is constrained within the die, the material deformation is hindered and the grain rotation blocked when the porosity is ejected. Under P_{SPS}=75 MPa, the sample (Fig. 4c) depicts porous zones imputable to the larger lateral pressure causing an antagonist effect to P_{SPS} one, thereby decreasing the bulk density to 98.5%. Full densification (99.2%) was achieved again under 100 MPa.

Since the Ca349 samples processed by SPS depicted a weak texture, the nano-indention was performed only in the direction parallel to the pressing axis to introduce the imprints on (*x*,*y*) plane of the samples. The average nH_{xy} and E_{xy} values considerably improve with P_{SPS} (Table 2). Increasing P_{SPS} from 0 to 30 MPa led nH_{xy} and E_{xy} to enhance from 0.11 ± 0.03 to 2.3 ± 0.1 GPa and from 10 ± 2 to 74 ± 3 GPa, respectively, due essentially to the density strengthening from 60% to 98.3%. Looking at the values of the maximum of the {001} poles, the texture seems to induce almost no effect. nH_{xy} and E_{xy} reveal a tiny increase afterward, elucidating the porosity in Ca349 samples are basically wiped out at low P_{SPS} range and major of densification is achieved under P_{SPS} not higher than 30 MPa; material densification becoming more and more difficult for higher P_{SPS} values. The densest sample (processed under

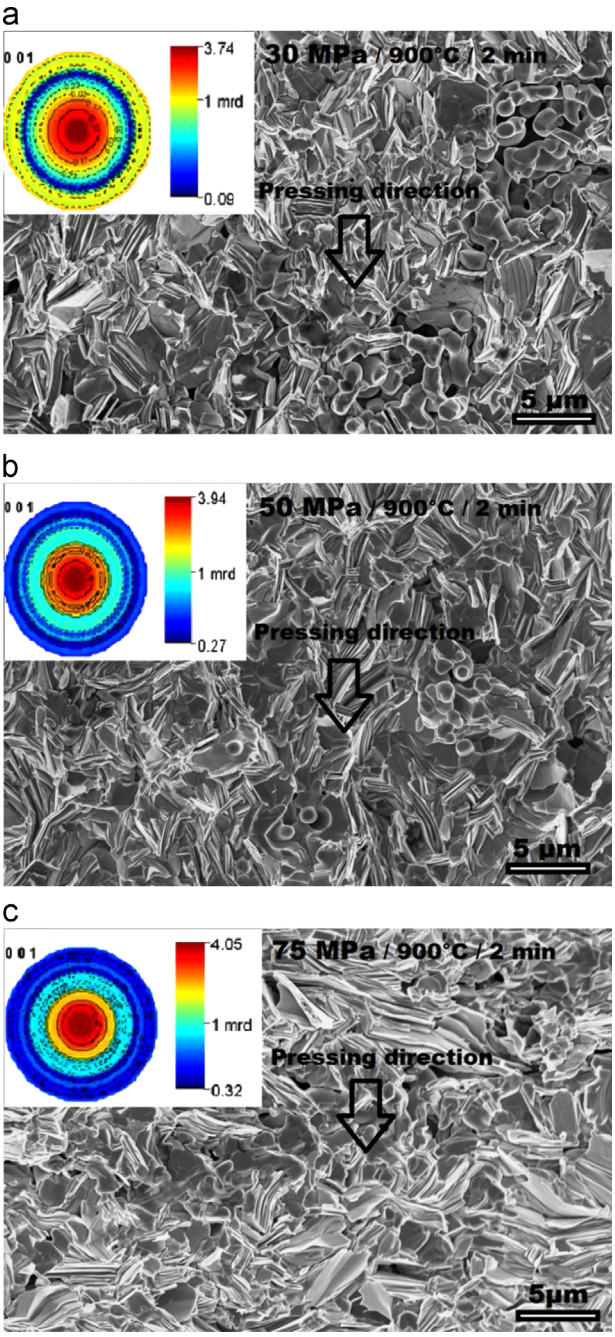

Fig. 4. SEM micrographs of fractured surfaces of spark plasma sintered Ca349 samples at 900 °C for 2 min and under (a) 30 MPa, (b) 50 MPa and (c) 75 MPa. Insets are the corresponding {010}, {001} and {100} pole figures.

100 MPa) depicts nH_{xy} value of 3.2 ± 0.4 GPa which is 26 fold the reference sample hardness and the largest achieved so far on Ca349 materials. This value is also more than 5 times that of the spark plasma sintered $CoSb_3$ and $LaFe_4Sb_{12}$ reported to be the hardest compounds of the skutterudite material family [47], and about 4 fold the TE material Bi_2Te_3 elaborated by SPS, already used in commercial TE modules [46]. Regarding the reported oxides treated by SPS, the largest value obtained for Ca349 materials is higher than that of $BaCeO_3$ and $SrCeO_3$ alkaline-earth perovskite oxides, similar to that of $BaMoO_3$ and lower than that of $BaZrO_3$, $BaUO_3$, $BaSnO_3$, $BaHfO_3$, $SrMoO_3$, $SrZrO_3$,

Table 2
Microstructural, textural and mechanical characteristics of the Ca349 materials consolidated by SPS under various applied uniaxial pressures P_{SPS} at 900 °C for 2 min.

Uniaxial pressure, P_{SPS} (MPa)	0	30	50	75	100
Microstructural–textural characteristics					
Relative percent densification (%)	60	90.3	99.6	98.5	99.2
Grain length (μm)	≤5	≤7	≤8	≤7	≤8
Max. of the {001} poles (mrd)	3.48	3.74	3.94	4.05	3.49
Mechanical characteristics					
nH_{xy} (GPa)	0.11 ± 0.03	2.34 ± 0.14	2.7 ± 0.3	3.1 ± 0.4	3.2 ± 0.5
E_{xy} (GPa)	10 ± 2	74 ± 3	82 ± 6	87 ± 5	86 ± 5
σ_R (MPa)	18.4 ± 0.5	252 ± 9	282 ± 7.7	250 ± 14	284 ± 8
K_{Ic} (MPa m$^{1/2}$)	0.40 ± 0.02	2.80 ± 0.09	2.92 ± 0.05	2.82 ± 0.1	2.77 ± 0.09

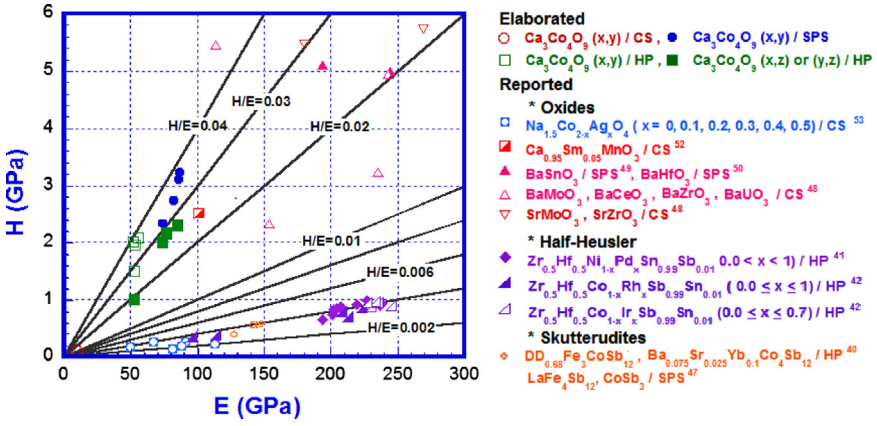

Fig. 5. *H/E* ratios for conventional sintered (CS), hot-pressed (HP) and spark plasma sintered (SPS) Ca349 materials compared to those reported for other oxide, skutterudite and half-Heusler materials.

$SrTiO_3$, $SrHfO_3$ and $SrRuO_3$ ones [48–50] although the Ca349 sample displays larger bulk density compared to the latters. The hardest alkaline-earth perovskite oxyde $SrRuO_3$ possesses hardness almost 4 fold the value of the hardest Ca349 sample.

E_{xy} ranges from 82 ± 6 to 86 ± 5 GPa for P_{SPS} larger or equal to 50 MPa and is then comparable to the one measured for the sample hot-pressed under 30 MPa, indicating that further densification brought by SPS compensates for the texture produced by HP. However, these values remain lower than those reported for the spark plasma sintered alkaline-earth perovskite oxydes [48–50], skutterudite compounds [47], or half-Heusler alloys [51].

The elastic recovery of materials has been shown to be reflected by the hardness to elastic modulus ratio *H/E*, a non-dimensional parameter commonly used for comparison of materials [39,41]. Fig. 5 compares to each other the elastic recoveries for Ca349 ceramics elaborated by using CS, HP and SPS, and to those of other bulk TE oxides and some TE material families reported to be potentially useful for energy conversion applications. First, one emphasizes that the oxides possess much larger elastic recovery compared to most other materials. The $(H/E)_{xy}$ ratio of Ca349 oxides processed by HP increases with P_{HP} and ranges from 0.0284 to 0.0373. A similar trend is also noted for the $(H/E)_z$ ratio which is lower and spans from 0.0188 to 0.0271 in the explored P_{HP} range, reflecting an elastic recovery anisotropy in the textured Ca349 oxides. The $(H/E)_{xy}$ ratios achieved on Ca349 oxides treated by SPS and HP are similar and more than 3 fold the reference sample value. Furthermore, they are one order of magnitude higher than *H/E* ratios obtained for half-Heusler alloys [41,42] or $Na_{1.5}Co_{2-x}Ag_xO_4$ oxides [53], prepared by HP and CS, respectively. They illustrate likewise almost similar *H/E* superiority when being compared to the skutterudites [40,47]. The *H/E* ratio is reported to vary from 0.0094 to 0.0299 for LAST compounds ($Ag_aPb_bSb_cTe_d$ with $0.006 \le a \le 0.043$, $0.417 \le b \le 0.480$, $0.011 \le c \le 0.50$ and $0.496 \le d \le 0.517$) [55,56] depending on their compositions, which is inferior or equal to those of our consolidated Ca349.

The hot-pressed and spark plasma sintered Ca349 oxides display larger elastic recovery than the perovskite oxides depicted in Fig. 5 whatever the processing method, except $SrMoO_3$ and $BaUo_3$ which show similar ($H/E = 0.0304$) and higher ($H/E = 0.0483$) ratios, respectively. We note as well that there are copper oxides (Sm_2CuO_4, Gd_2CuO_4, Nd_2CuO_4) [54] possessing similar *H/E* values, and the highest reported *H/E* ratios are for the oxides $Ca_{0.95}Sm_{0.05}MnO_3$ ($H/E = 0.0539$) [52] and $SrRuO_2$ ($H/E = 0.0789$) [48] treated by SPS and CS, respectively.

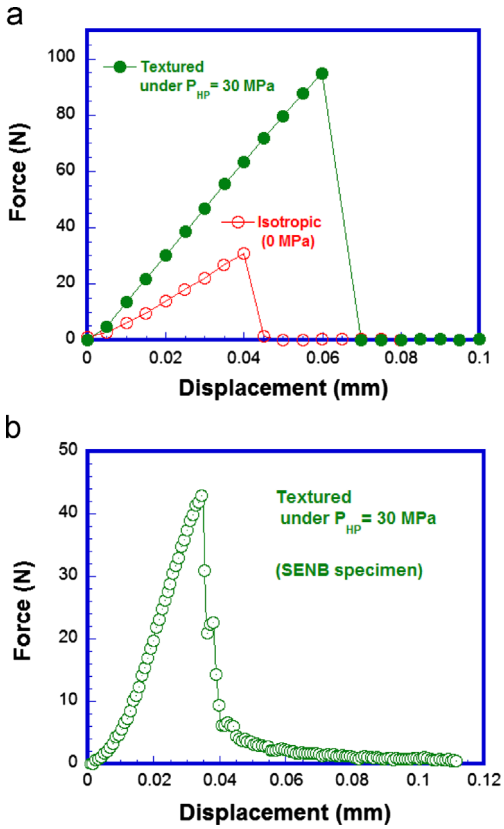

Fig. 6. (a) 3 point bending loading diagram of two smooth Ca349 ceramics tested in flat-wise orientation: the isotropic sample (reference) and the one textured by HP under 30 MPa. (b) The texture effect on the 3 point bending loading diagram of SENB specimen initially processed by HP under 30 MPa.

3.2. Fracture characteristics

Fig. 6a presents the 3 point bending loading diagram of two smooth Ca349 ceramics: the isotropic sample (reference) and the one textured by HP under 30 MPa. The tests were performed in flat-wise orientation, i.e. the loading direction was parallel to the pressing axis. The diagrams outline the brittle behavior of these ceramics and evidence two main domains: (i) a linear portion corresponding to the elastic behavior till the maximum load, and (ii) a much narrower domain of catastrophic crack propagation. For the textured samples, when the platelets are perpendicular to the loading axis, the crack is deflected from its initial plane by the interfaces between them. The fracture proceeds by transgranular rupture of the platelets and crack deflection at grain boundaries.

The fracture stress (or strength) σ_R of the Ca349 bulk materials was found to depend on the uniaxial pressure applied during the sintering for both processing methods (HP or SPS, see Tables 1 and 2). The strength σ_R shows a similar trend to the one of hardness and elastic modulus: it records an increase of more than one order of magnitude upon hot-pressing under only 5 MPa and then reached 249 ± 4 MPa for P_{HP}=30 MPa, which 2 fold the value reported for Bi_2Te_3 bulk materials [48,57].

A similar enhancement in σ_R was noted for the samples treated by SPS under an equivalent pressure. The materials prepared under higher P_{SPS} of 50 MPa were found to possess strength as high as 282 ± 8 MPa, i.e. 15 times the reference material. To our knowledge, this is the largest strength obtained so far on Ca349 bulk materials.

Increasing P_{SPS} to 75 MPa causes the strength to drop by 11%, which is well correlated to the presence of weakly dense zones noted on the corresponding microstructure (Fig. 4c). In contrast, these strength shortfalls were not observed when P_{SPS} was further increased to 100 MPa, which is consistent with the density level noted on the corresponding specimen (Table 2).

Importantly, although the Young's modulus, E, was not impaired by these defected areas, SPS processing in its classical configuration with pressure larger than 50 MPa proves to be harmful toward some critical mechanical characteristics of Ca349 bulk materials. Likewise, samples elaborated in such processing conditions revealed a worsening of the TE porperties [22]. Nonetheless, we have recently reported an amended SPS configuration, referred to as edge-free spark plasma sintering or spark plasma texturing (SPT), enabling a free deformation of the grains perpendicular to the pressing axis, thereby preventing defected areas and, concomitantly, inducing a rapid material texturation [58].

Fig. 6b shows the texture effect on the 3 point bending loading curve of a SENB specimen, processed by HP under 30 MPa, tested in flat-wise orientation. Beyond the maximum load, the crack propagates in a more or less controlled manner reflecting the successive ruptures of stacked platelets.

The HP processing was found to be highly effective for enhancing the resistance of Ca349 ceramics to crack propagation from a major flaw. Compared to the isotropic ceramic (reference), the fracture toughness K_{Ic} recorded a significant increase factor of 4.7 upon HP under P_{HP}=5 MPa. This factor monotonously increased with P_{HP} to reach 5.7 for P_{HP} of 30 MPa, which is derived from the material densification, texture strengthening and diminishing in the (x,y) plane GBD.

The SPS processing fosters superior resistance to crack propagation in Ca349 ceramics. Indeed, a higher improvement (more than 7 times) was obtained in K_{Ic} under pressure P_{SPS} of 30 MPa, and is ascribed to the fully material densification. K_{Ic} topped at 2.92 ± 0.05 MPa $m^{1/2}$ for P_{SPS} of 50 MPa, the material with the highest bulk density. As with the strength σ_R, K_{Ic} slightly drops for larger P_{SPS} values, in keeping with the microstructure features (Fig. 4c). SEM observations showed that failure proceeds by intergranular cracking.

With the aim to evaluate the size of the intrinsic flaws in the samples processed by CS, HP and SPS, we made use of Eq. 6. Assuming that the intrinsic flaws are small, the strength σ_R measured on smooth Ca349 ceramics was used and the shape factor Y was set equal to $\sqrt{\pi}$. Fig. 7 shows the evolution of the intrinsic flaw size versus the applied pressure P_{SPS}. While the isotropic sample depicts the largest intrinsic flaws (150 μm) which are likely the pores resulting from the weak densification (60% of the theoretical density), the flaw size considerably drops as the uniaxial pressure P_{SPS} is applied. Furthermore, the intrinsic flaw size does not seem to depend on the pressure

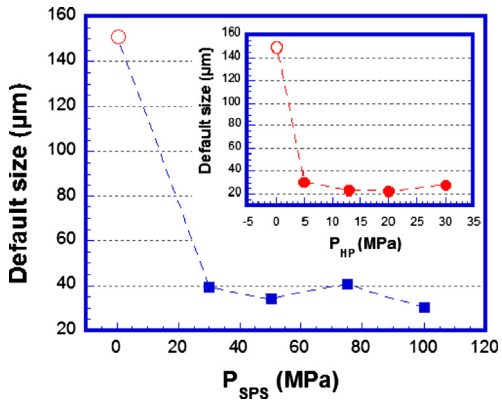

Fig. 7. The effect of CS, HP and SPS treatments on the size of major flaw a^* in Ca349 ceramics.

(same for P_{HP} shown in the inset). Despite higher densification is achieved by SPS processing, HP treatment results in smaller intrinsic flaws, probably linked to the higher grain orientation by this process (Fig. 3e) while in SPS the disorientation between grains is much more pronounced (Fig. 4). For the same applied pressure of 30 MPa, HP processing leads to lower fracture toughness (2.30 MPa $m^{1/2}$) than SPS (2.80 MPa $m^{1/2}$). That may be ascribed to the higher GBD in the $(x,z)/(y,z)$ planes (the grains are thinner) in the materials treated by HP (Table 1). We note an increase in flaws size for P_{SPS} of 75 MPa in accordance with the microstructure observation (Fig. 4c), and for P_{HP} of 30 MPa probably due to the cracking of the thinner grains.

4. Conclusions

Micro-hardness (μH), nano-hardness (nH), elastic modulus (E), strength (σ_R) and fracture toughness (K_{Ic}) were assisted for $Ca_3Co_4O_9$ (Ca349) bulk oxides initially processed by using Hot-Pressing (HP) and Spark Plasma Sintering (SPS) toward the optimization of their thermoelectric (TE) properties. These mechanical characteristics were shown to be drastically fostered under the effects of both processes. They are the largest for Ca349 materials fully densified by SPS under $P_{SPS} \geq 50$ MPa with $nH_{xy} = 3.2 \pm 0.5$ GPa, $E_{xy} = 87 \pm 5$ GPa, $\sigma_R = 284 \pm 8$ MPa, and $K_{Ic} = 2.82 \pm 0.4$ MPa $m^{1/2}$, corresponding to more than 29, 8, 15 and 6 fold the conventional sintered (CS) ceramics often used in TE devices. Although Ca349 ceramics treated by HP were found to depict lower mechanical characteristics, they remain however drastically more reliable compared to the CS ones. We note that the hot-pressed Ca349 materials were reported to possess the best TE performances as well, which makes them most suitable for being used in TE devices. The elastic recovery H/E of Ca349 materials processed by HP and SPS can reach 0.04, which is more than one order of magnitude larger compared to the half-Heusler or skutterudites promising candidates for TE applications.

Acknowledgments

Driss Kenfaui and the authors acknowledge the “Conseil Régional de Basse-Normandie, France” for the fellowship and financial participation for experimental set-up used in this work. The authors thank also Mr. Jean-Pierre Burnouf and Mr. Julien Poughon for their help during the material preparation.

References

[1] G. Jeffrey Snyder, E.S. Toberer, Complex thermoelectric materials, Nat. Mater. 7 (2008) 105–114.
[2] S.M. Kauzlarich, S.R. Brown, G. Jeffrey Snyder, Zintl phases for thermoelectric devices, Dalton Trans. (2007) 2099–2107.
[3] E.J. Winder, A.B. Ellis, G.C. Lisensky, Thermoelectric devices: solid-state refrigerators and electrical generators in the classroom, J. Chem. Educ. 73 (10) (1996) 940–946.
[4] G.A. Slack, in: D.M. Rowe (Ed.), CRC Handbook of Thermoelectrics, CRC Press, New York, 1995, pp. 407–440.
[5] J.W. Fergus, Oxide materials for high thermoelectric energy conversion, J. Eur. Ceram. Soc. 32 (2012) 525–540.
[6] K. Koumoto, I. Terasaki, R. Funahashi, Complex oxide materials for potential thermoelectric applications, Mater. Res. Soc. Bull. 31 (2006) 206–210.
[7] F.J. DiSalvo, Thermoelectric cooling and power generation, Science 285 (1999) 703–706.
[8] M.S. Dresselhaus, G. Chen, M.Y. Tang, R.G. Yang, H. Lee, D.Z. Wang, Z.F. Ren, J.-P. Fleurial, P. Gogna, New directions for low-dimensional thermoelectric materials, Adv. Mater. 19 (2007) 1043–1053.
[9] B.C. Sales, Electron crystals and phonon glasses: a new path to improved thermoelectric materials, Mater. Res. Soc. Bull. 23 (1998) 15–21.
[10] F.D. Rosi, E.F. Hockings, N.E. Lindenblad, Semiconducting materials for thermoelectric power generation, RCA Rev. 22 (1961) 82–121.
[11] C. Wood, Materials for thermoelectric energy-conversion, Rep. Prog. Phys. 51 (1988) 459–539.
[12] S. Li, R. Funahashi, I. Matsubara, K. Ueno, H. Yamada, High temperature thermoelectric properties of oxide $Ca_9Co_{12}O_{28}$, J. Mater. Chem. 9 (1999) 1659–1660.
[13] A.C. Masset, C. Michel, A. Maignan, M. Hervieu, O. Toulemonde, F. Studer, B. Raveau, J. Hejtmanek, Misfit-layered cobaltite with an anisotropic giant magnetoresistance: $Ca_3Co_4O_9$, Phys. Rev. B 62 (2000) 166–175.
[14] C.H. Lim, S.-M. Choi, W.-S. Seo, H.-H. Park, A power-generation test for oxide-based thermoelectric modules using p-type $Ca_3Co_4O_9$ and n-type $Ca_{0.9}Nd_{0.1}MnO_3$ legs, J. Electron. Mater. 41 (2012) 1247–1255.
[15] S.-M. Choi, K.-H. Lee, C.-H. Lim, W.-S. Seo, Oxide-based thermoelectric power generation module using p-type $Ca_3Co_4O_9$ and n-type $(ZnO)_7In_2O_3$ legs, Energy Convers. Manag. 52 (2011) 335–339.
[16] J.G. Noudem, S. Lemonnier, M. Prevel, E.S. Reddy, E. Guilmeau, C. Goupil, Thermoelectric ceramics for generators, J. Eur. Ceram. Soc. 28 (2008) 41–48.
[17] R. Funahashi, S. Urata, Fabrication and application of an oxide thermoelectric system, Int. J. Appl. Ceram. Technol. 4 (2007) 297–307.
[18] E. Sudhakar Reddy, J.G. Noudem, S. Hébert, C. Goupil, Fabrication and properties of four-leg oxide thermoelectric modules, J. Phys. D: Appl. Phys. 38 (2005) 3751–3755.
[19] D. Kenfaui, D. Chateigner, M. Gomina, J. Noudem, Texture, mechanical and thermoelectric properties of $Ca_3Co_4O_9$ ceramics, J. Alloys Compd. 490 (2010) 472–479.
[20] J.G. Noudem, D. Kenfaui, D. Chateigner, M. Gomina, Granular and lamellar thermoelectric oxides consolidated by spark plasma sintering, J. Electron. Mater. 40 (2011) 1100–1106.
[21] J.Y. Zeng, Y. Sato, C. Ohkubo, T. Hosoi, In vitro wear resistance of three types of composite resin denture teeth, J. Prosthet. Dent. 94 (2005) 453.
[22] P.V. Krakhmalev, J. Bergstrom, Tribological behavior and wear mechanisms of $MoSi_2$-base composites sliding against AA6063 alloy at elevated temperature, Wear 260 (2006) 450.

[23] K. Morita, A. Umenzawa, S. Yamato, A. Makishima, Surface roughness of yttria-containing aluminosilicate glass–ceramics as indicative of their machinability, J. Am. Ceram. Soc. 76 (1993) 1861.
[24] R.K. Kamboj, S. Dhara, P. Bhargava, Machining behaviour of green gelcast ceramics, J. Eur. Ceram. Soc. 23 (2003) 1005.
[25] R. Wang, W. Pan, M. Jiang, J. Chen, Y. Luo, Investigation of the physical and mechanical properties of hot-pressed machinable Si3N4/h-BN composites and FGM, Mater. Sci. Eng. B 90 (2002) 261.
[26] R.W. Rice, Mechanical Properties of Ceramics and Composites, Marcel Dekker, New York, 2000, p. 308–312.
[27] R.W. Rice, The Compressive Strength of Ceramics, Materials Science Research, in: W. Wurth, Hayne Palmour Kriegel III (Eds.), Ceramics in Severe Environments, vol. 5, Plenum, New York, 1971, pp. 195–229.
[28] B.R. Lawn, Fracture of Brittle Solids, second ed., Cambridge University Press, New York, 1993, p. 258–263.
[29] D.B. Marshall, T. Noma, A.G. Evans, A simple method for determining elastic-modulus–to-hardness ratios using Knoop indentation measurements, Am. Ceram. Soc. Bull. 65 (1982) C175.
[30] D. Kenfaui, B. Lenoir, D. Chateigner, B. Ouladdiaf, M. Gomina, J.G. Noudem., Development of multilayer textured $Ca_3Co_4O_9$ materials for thermoelectric generators: influence of the anisotropy on the transport properties, J. Eur. Ceram. Soc. 32 (2012) 2405–2414.
[31] D. Kenfaui, G. Bonnefont, D. Chateigner, G. Fantozzi, M. Gomina, J.G. Noudem, $Ca_3Co_4O_9$ ceramics consolidated by SPS process: optimization of mechanical and thermoelectric properties, Mater. Res. Bull. 45 (2010) 1240–1249.
[32] J. Ricote, D. Chateigner, Quantitative texture analysis applied to the study of preferential orientations in ferroelectric thin films, Bol. Soc. Esp. Ceram. Vidrio 38 (1999) 587–591.
[33] D. Chateigner, Combined Analysis, Wiley-ISTE, New York, 2010, p. 496.
[34] Matthies Lutterotti, Wenk, MAUD (Material Analysis Using Diffraction): A User Friendly Java Program for Rietveld Texture Analysis and More, in: J.A. Spunar (Ed.), National Research Council of Canada, Ottawa, 1999, pp. 1599–1604.
[35] L. Lutterotti, D. Chateigner, S. Ferrari, J. Ricote, Texture, residual stress and structural analysis of thin films using a combined X-ray analysis, Thin Solid Films 450 (2004) 34–41.
[36] E. Guilmeau, D. Chateigner, J. Noudem, R. Funahashi, S. Horii, B. Ouladdiaf, Rietveld texture analysis of complex oxides: examples of polyphased Bi2223 superconducting and Co349 thermoelectric textured ceramics characterization using neutron and X-ray diffraction, J. Appl. Cryst. 38 (2005) 199–210.
[37] J.B. Wachtman, Mechanical Properties of Ceramics, Wiley and Sons, New York, Inc., 1996.
[38] J. Woirgard, J.C. Daegenton, An alternative method for penetration depth determination in nanoindentation measurement, J. Mater. Res. 12 (1997) 2455–2458.
[39] W.C. Oliver, G.M. Pharr, An improved technique for determining hardness and elastic modulus using load and sensing indentation experiments, J. Mater. Res. 7 (1992) 1564–1583.
[40] L. Zhang, G. Rogl, A. Grystiv, S. Puchegger, J. Koppensteiner, F. Spiekermann, H. Kabelka, M. Reinecker, P. Rogl, W. Schranz, M. Zehetbauer, M.A. Carpenter, Mechanical properties of filled antimonide skutterudites, Mater. Sci. Eng. B 170 (2010) 26.
[41] M.A. Verges, P.J. Schilling, P. Upadhyay, W.K. Miller, R. Yaqub, K. L. Stokes, P.F.P. Poudeu, Young's modulus and hardness of $Zr_{0.5}Hf_{0.5}Ni_xPd_{1-x}Sn_{0.99}Sb_{0.01}$ half-Heusler compounds, Sci. Adv. Mater. 3 (2011) 659–666.
[42] M.A. Verges, P.J. Schilling, J.D. Germond, P. Upadyhay, W.K. Miller, P. Maji, N.J. Takas, P.F.P. Poudeu, Young's modulus and hardness of $Zr_{0.5}Hf_{0.5}Co_xRh_{1-x}Sb_{0.99}Sn_{0.01}$ and $Zr_{0.5}Hf_{0.5}Co_xIr_{1-x}Sb_{0.99}Sn_{0.01}$ half-Heusler alloys, in: Proceedings of the ASME 2010 International Mechanical Engineering Congress and Exposition, Vancouver, Canada, November 2010, vol. IMECE2010-38988.
[43] Q. Yang, W. Lengauer, T. Koch, M. Scheerer, I. Smid, Hardness and elastic properties of $Ti(C_xN_{1-x})$, $Zr(C_xN_{1-x})$ and $Hf(C_xN_{1-x})$, J. Alloys Compd. 309 (2000) L5–L9.
[44] A. Kosuga, M. Uno, K. Kurosaki, S. Yamanaka, Thermoelectric properties of stoichiometric $Ag_{1-x}Pb_{18}SbTe_{20}$ ($x=0$, 0.1, 0.2), J. Alloys Compd. 387 (2005) 52.
[45] R.D. Schmidt, J.E. Ni, E.D. Case, J.S. Sakamoto, D.C. Kleinkow, B. L. Wing, R.C. Stewart, E.J. Timm, Room temperature Young's modulus, shear modulus, and Poisson's ratio of $Ce_{0.9}Fe_{3.5}Co_{0.5}Sb_{12}$ and $Co_{0.95}Pd_{0.05}Te_{0.05}Sb_3$ skutterudite materials, J. Alloys Compd. 504 (2010) 303.
[46] L.-D. Zhao, B.-P. Zhang, J.-F. Li, M. Zhou, W.-S. Liu, J. Liu, Thermoelectric and mechanical properties of nano-SiC-dispersed Bi_2Te_3 fabricated by mechanical alloying and spark plasma sintering, J. Alloys Compd. 455 (2008) 259–264.
[47] C. Recknagel, N. Reinfried, P. Hohn, W. Schnelle, H. Rosner, Y. Grin, A. Leithe-Jasper, Application of spark plasma sintering to the fabrication of binary and ternary skutterudites, Sci. Tech. Adv. Mater. 8 (2007) 357.
[48] S. Yamanaka, K. Kurosaki, T. Maekawa, T. Matsuda, S. Kobayashi, M. Uno, Thermochemical and thermophysical properties of alkaline-earth perovskites, J. Nucl. Mater. 344 (2005) 61–66.
[49] T. Maekawa, K. Kurosaki, S. Yamanaka, Thermal and mechanical properties of polycrystalline $BaSnO_3$, J. Alloys Compd. 416 (2006) 214–217.
[50] T. Maekawa, K. Kurosaki, S. Yamanaka, Thermal and mechanical properties of perovskite-type barium hafnate, J. Alloys Compd. 407 (2006) 44–48.
[51] T. Sekimoto, K. Kurosaki, H. Muta, S. Yamanaka, Thermoelectric and thermophysical properties of ErPdX (X=Sb and Bi) half-Heusler compounds, J. Appl. Phys. 99 (2006) 103701.
[52] J.G. Noudem, D. Kenfaui, S. Quetel-Weben, C.S. Sanmathi, R. Retoux, M. Gomina, Spark plasma sintering of n-type thermoelectric $Ca_{0.95}Sm_{0.05}MnO_3$, J. Am. Ceram. Soc. 94 (8) (2011) 2608–2612.
[53] T. Seetawan, V. Amornkitbamrung, T. Burinprakhon, S. Maensiri, K. Kurosaki, H. Muta, M. Uno, S. Yamanaka, Mechanical properties of Ag-doped $Na_{1.5}Co_2O_4$, J. Alloys Compd. 403 (2005) 308–311.
[54] S. Yamanaka, H. Kobayashi, K. Kurosaki, Thermophysical properties of layered rare earth copper oxides, J. Alloys Compd. 349 (2003) 269.
[55] F. Ren, E.D. Case, E.J. Timm, H.J. Schock, Hardness as a function of composition for n-type LAST thermoelectric material, J. Alloys Compd. 455 (2008) 340.
[56] F. Ren, E.D. Case, E.J. Timm, H.J. Schock, Young's modulus as a function of composition for an n-type lead–antimony–silver–telluride (LAST) thermoelectric material, Philos. Mag. 87 (2007) 4907.
[57] L.D. Zhao, B.-P. Zhang, J.-F. Li, H.L. Zhang, W.S. Liu, Enhanced thermoelectric and mechanical properties in textured n-type Bi_2Te_3 prepared by spark plasma sintering, Sol. State Sci. 10 (2008) 651–658.
[58] J.G. Noudem, D. Kenfaui, D. Chateigner, M. Gomina, Toward the enhancement of thermoelectric properties of lamellar $Ca_3Co_4O_9$ by edge-free spark plasma texturing, Scr. Mater. 66 (2012) 258–260.